

## ARTICLE

Received 21 Mar 2014 | Accepted 11 Sep 2014 | Published 18 Nov 2014

DOI: 10.1038/ncomms6246

# Strain and structure heterogeneity in MoS<sub>2</sub> atomic layers grown by chemical vapour deposition

Zheng Liu<sup>1,2,3,\*</sup>, Matin Amani<sup>4,\*</sup>, Sina Najmaei<sup>5,\*</sup>, Quan Xu<sup>6,7</sup>, Xiaolong Zou<sup>5</sup>, Wu Zhou<sup>8</sup>, Ting Yu<sup>9</sup>, Caiyu Qiu<sup>9</sup>, A Glen Birdwell<sup>4</sup>, Frank J. Crowne<sup>4</sup>, Robert Vajtai<sup>5</sup>, Boris I. Yakobson<sup>5</sup>, Zhenhai Xia<sup>6</sup>, Madan Dubey<sup>4</sup>, Pulickel M. Ajayan<sup>5</sup> & Jun Lou<sup>5</sup>

Monolayer molybdenum disulfide (MoS<sub>2</sub>) has attracted tremendous attention due to its promising applications in high-performance field-effect transistors, phototransistors, spintronic devices and nonlinear optics. The enhanced photoluminescence effect in monolayer MoS<sub>2</sub> was discovered and, as a strong tool, was employed for strain and defect analysis in MoS<sub>2</sub>. Recently, large-size monolayer MoS<sub>2</sub> has been produced by chemical vapour deposition, but has not yet been fully explored. Here we systematically characterize chemical vapour deposition-grown MoS<sub>2</sub> by photoluminescence spectroscopy and mapping and demonstrate non-uniform strain in single-crystalline monolayer MoS<sub>2</sub> and strain-induced bandgap engineering. We also evaluate the effective strain transferred from polymer substrates to MoS<sub>2</sub> by three-dimensional finite element analysis. Furthermore, our work demonstrates that photoluminescence mapping can be used as a non-contact approach for quick identification of grain boundaries in MoS<sub>2</sub>.

<sup>1</sup>School of Materials Science and Engineering, Nanyang Technological University, Singapore 639798, Singapore. <sup>2</sup>NOVITAS, Nanoelectronics Centre of Excellence, School of Electrical and Electronic Engineering, Nanyang Technological University, Singapore 639798, Singapore. <sup>3</sup>CINTRA CNRS/NTU/THALES, UMI 3288, Research Techno Plaza, 50 Nanyang Drive, Border X Block, Level 6, Singapore 637553, Singapore. <sup>4</sup>Sensors and Electron Devices Directorate, US Army Research Laboratory, Adelphi, Maryland 20783, USA. <sup>5</sup>Department of Materials Science and Nanoengineering, Rice University, Houston, Texas 77005, USA. <sup>6</sup>Department of Materials Science and Engineering, University of North Texas, 1155 Union Circle, Denton, Texas 76203, USA. <sup>7</sup>Institute of New Energy, China University of Petroleum (Beijing), Beijing 102200, China. <sup>8</sup>Materials Science & Technology Division, Oak Ridge National Lab, Oak Ridge, Tennessee 37831, USA. <sup>9</sup>Division of Physics and Applied Physics, School of Physical and Mathematical Sciences, Nanyang Technological University, Singapore 637371, Singapore. \* These authors contributed equally to this work. Correspondence and requests for materials should be addressed to J.L. (email: jlou@rice.edu) or to P.M.A. (email: ajayan@rice.edu) or to M.D. (email: madan.dubey.civ@mail.mil).

High-quality and single-layered molybdenum disulfide ( $\text{MoS}_2$ ) has been synthesized by chemical vapour deposition (CVD) over the past 2 years<sup>1–9</sup>, boosting its promise in applications involving hydrogen evolution reaction<sup>10</sup>, supercapacitors<sup>11</sup>, ultra-low power consumption field-effect transistors and phototransistor<sup>12,13</sup>, spintronic devices<sup>14</sup>, nonlinear optics<sup>15</sup> and biosensors<sup>16</sup>. CVD-grown  $\text{MoS}_2$  atomic layers are also superior to samples prepared by mechanical exfoliation and chemical isolation methods, as continuous monolayer  $\text{MoS}_2$  (hereafter 1H- $\text{MoS}_2$ ) can currently be grown at the centimetre-length scale<sup>3,11,17,18</sup>. However, concurrently with the large-scale growth of monolayer  $\text{MoS}_2$ , variations in crystal geometries and atomic structures have been predicted and observed<sup>19</sup>. Geometrically,  $\text{MoS}_2$  triangles, hexagons, six-pointed stars, irregular shapes and continuous films can be synthesized, depending on the precise growth conditions such as pressure, temperature, substrates, precursors, cooling rate and so on<sup>3–5,18,20</sup>. Structurally, like graphene, a wide variety of grain boundaries (GBs) has been observed in polycrystalline CVD-grown  $\text{MoS}_2$  (refs 3,4,21). Thus, it is important to understand how these variations modify the physical properties of  $\text{MoS}_2$ .

It is well known that  $\text{MoS}_2$  has an indirect-to-direct bandgap transition as it is thinned down from multi-layer to monolayer, producing a significant enhancement of photoluminescence (PL) quantum yield as a result of the direct bandgap excitonic transition<sup>22,23</sup>. However, the intensities and peak positions of such PL signals closely correlate with many other parameters

such as crystal structure, local doping and strain within the sample and require more detailed examination. CVD-grown  $\text{MoS}_2$  with the richness of its intrinsic and extrinsic defects show significant heterogeneity in PL characteristics. Consequently, a systematic examination of PL characteristics in CVD-grown  $\text{MoS}_2$  could provide information to help better understand the growth mechanisms, crystal structure and band structure of these monolayers.

In this work we examine the PL characteristics of CVD-grown  $\text{MoS}_2$  monolayers with a focus on the role of growth-induced non-uniform strain and GBs. We examine the PL intensity and peak position variations observed in different samples and explore the possible contributions to such changes. We find that non-uniform tensile strain is intrinsic to CVD-grown  $\text{MoS}_2$  on  $\text{SiO}_2$  and such strain variation can be identified by PL mapping. Such strain is induced through interactions with the  $\text{SiO}_2$  substrate and can be released after transferring  $\text{MoS}_2$  to other substrates. On the other hand, controlled tensile strain could be purposely introduced to monolayer  $\text{MoS}_2$  by stretching the deformable substrates it sits on, therefore providing an effective method for bandgap engineering. To understand the role of substrate properties on effective strain transfer and corresponding band structure changes in  $\text{MoS}_2$ , three-dimensional (3D) finite element analysis (FEA) and DFT calculations were performed. These results indicate that substrates with high Young's modulus can dramatically reduce the strain loss during tensile experiments, while the commonly used polydimethylsiloxane (PDMS) can only

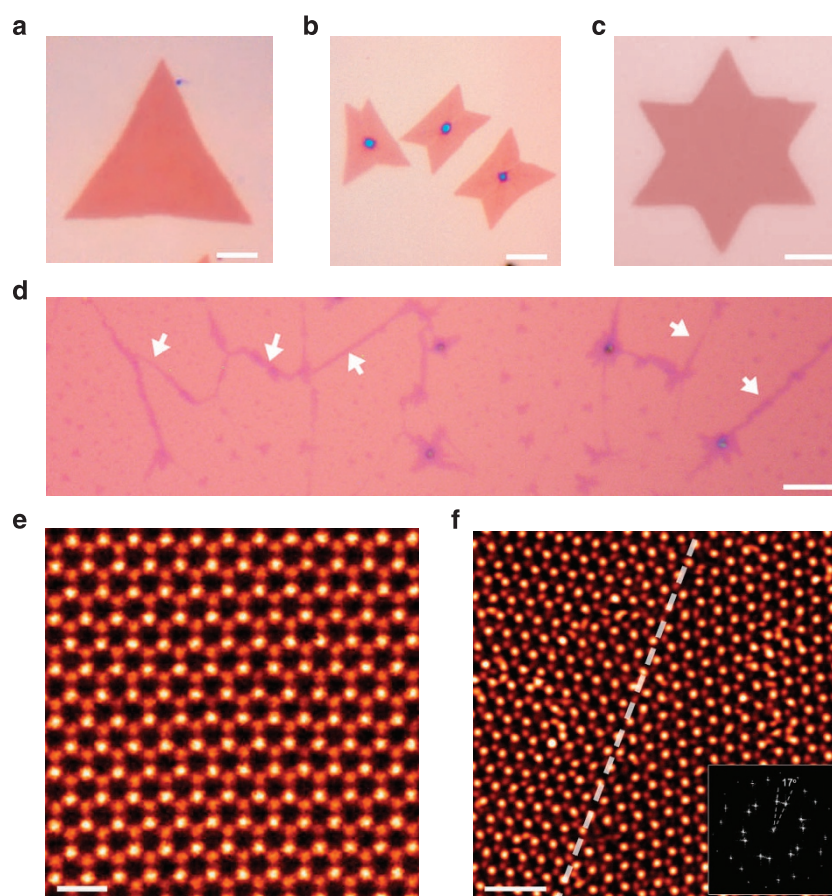


**Figure 1 | Geometries and atomic structures of CVD-grown monolayer  $\text{MoS}_2$ .** (a–c) Optical images of (a) single-crystal  $\text{MoS}_2$  triangle, (b) polycrystalline  $\text{MoS}_2$  with nucleation sites located at the centre and (c) polycrystalline six-pointed  $\text{MoS}_2$  star. Scale bar, 5, 10 and 5  $\mu\text{m}$ , respectively. (d) Optical image of a  $\text{MoS}_2$  film with second-layer  $\text{MoS}_2$  stripes grown along the GBs, indicated by the white arrows. Scale bar, 5  $\mu\text{m}$ . (e) Annular dark-field scanning TEM image of defect-free  $\text{MoS}_2$ . Scale bar, 0.5 nm. (f) Grain boundary in  $\text{MoS}_2$  with a rotation angle of  $\sim 17^\circ$ . The grain boundary is highlighted by the white dash line. Scale bar, 1 nm.

transfer  $\sim 10\%$  tensile strain to  $\text{MoS}_2$ . Finally, examination of line defects in monolayer  $\text{MoS}_2$  samples shows that GBs can modulate the PL response of the material in ways different from what has been previously proposed. This not only gives insight into mechanisms of PL modulation at the GBs but also exemplifies a technique superior to dark-field imaging in transmission electron microscopy (TEM) for their non-destructive visualization in  $\text{MoS}_2$  monolayers.

## Results

**Sources of PL heterogeneity in CVD-grown  $\text{MoS}_2$ .** To explore the heterogeneity in CVD-grown  $\text{MoS}_2$  atomic layers, we synthesize  $\text{MoS}_2$  single-crystal and polycrystalline films using  $\text{MoO}_3$  nanoribbons and sublimated sulfur as the sources for Mo and S, respectively, and react at a temperature of  $\sim 850^\circ\text{C}$  followed by a fast-cooling phase (see Methods)<sup>4</sup>. The growth of large-area films has been proven to be a process of nucleation, growth and coalescence of single-crystalline triangular domains. More importantly, the formation of these films is nucleation limited, and using pristine silicon dioxide substrates, one can truncate the process to form isolated single crystals. Our experiments show that the configuration and position of the  $\text{MoO}_3$  relative to the designated growth substrate is critical to the shape and structure of the as-grown crystals. As a result, one can promote the growth of polycrystalline flakes and continuous films with unique geometries suitable for comprehensive study of PL in  $\text{MoS}_2$  (Fig. 1a–d).

Some general features of the  $\text{MoS}_2$  flakes and films grown using this method are shown in Fig. 1, such as single-crystal triangular  $\text{MoS}_2$  flake (Fig. 1a), irregular  $\text{MoS}_2$  shapes (Fig. 1b), symmetric six-pointed  $\text{MoS}_2$  star (Fig. 1c) and polycrystalline  $\text{MoS}_2$  films (Fig. 1d). The bright areas located at the centre of  $\text{MoS}_2$  layers (Fig. 1b) are the original nucleation sites for the crystals. The quality of the CVD-grown  $\text{MoS}_2$  is comparable to that of the exfoliated samples, which has been confirmed by multiple characterization techniques<sup>4</sup>. The perfect lattice of monolayer  $\text{MoS}_2$  (Fig. 1e) can be seen from the annular dark-field scanning TEM imaging. The brighter atomic sites are Mo atoms, while the weaker ones are double-S columns. GBs are also found in the CVD-grown  $\text{MoS}_2$  (Fig. 1f) with many variations as discussed in our previous work<sup>4,21</sup>. For large-area films, some GBs are observed from the optical images where a second-layer  $\text{MoS}_2$  tends to grow along the GBs, resulting in dark purple stripes indicated by the white arrows (Fig. 1d). Typical Raman spectra and intensity mapping from these mono-/bilayer topographies are shown in the Supplementary Fig. 1. These features indicate that GBs are preferred sites for nucleation of second layers. However, these optically identifiable features do not fully account for all the GBs present in the samples (Fig. 1b,c). PL characterization of these typical crystals can provide more information about distinctive features of different growth modes due to the enhanced intensity of monolayer  $\text{MoS}_2$  (ref. 22).

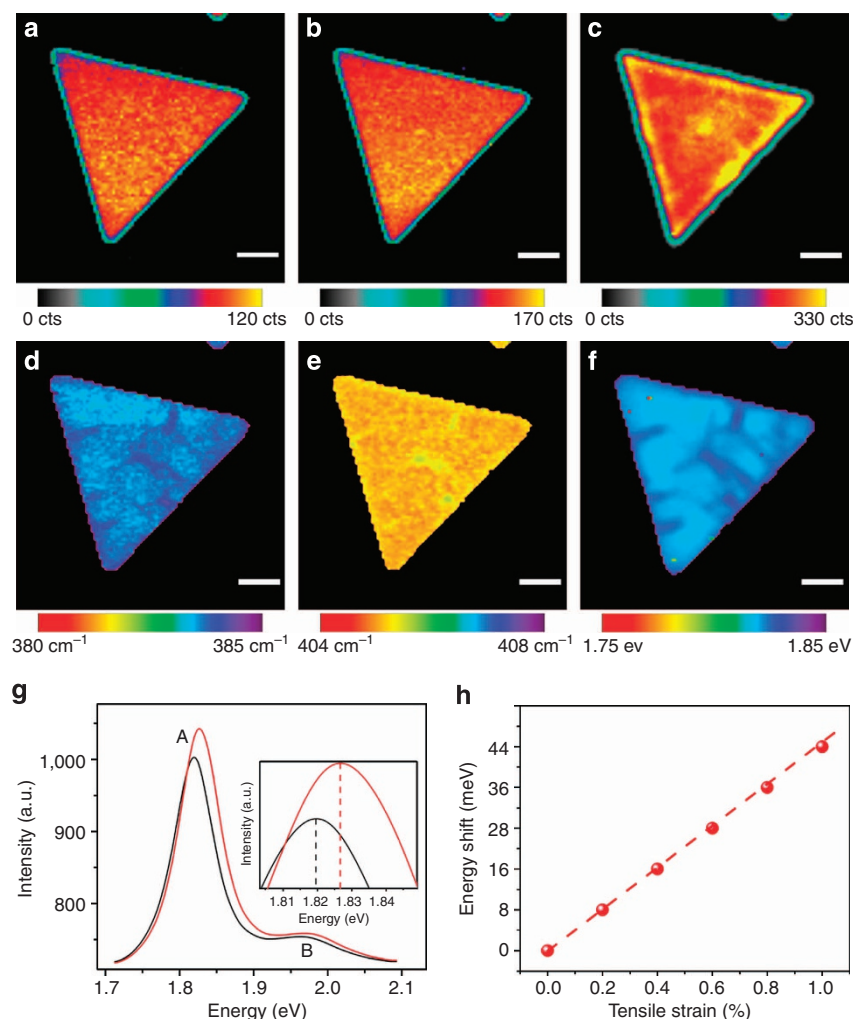
## Native strain variations in CVD-grown $\text{MoS}_2$ monolayers.

Figure 2 presents high-resolution Raman and PL mapping of a  $\text{MoS}_2$  triangular single crystal, acquired with long integration times to observe subtle shifts in the signal. Raman mapping of the  $E_{2g}^1$  and  $A_{1g}$  peaks shows a uniform intensity (with  $<5\%$  variation) over the triangle (Fig. 2a,b). However, significant variations are seen in the PL intensity mapping (Fig. 2c) and it can be seen that the edges and some regions within the triangles have up to a  $\sim 200\%$  higher intensity. Raman and PL peak position mapping provide images with better contrast. Clear lines related to the shift in peak positions ( $\sim 1.0\text{ cm}^{-1}$  hardening in  $E_{2g}^1$  and  $0.4\text{ cm}^{-1}$  in  $A_{1g}$ ) can be observed (Fig. 2d,e). More interestingly,

the best contrast is seen in the PL peak position mapping (blue lines in Fig. 2f) along and perpendicular to the edges, corresponding to a blue shift of  $\sim 8\text{ meV}$  (Fig. 2g). We propose that these characteristics may arise from the growth process that ends with a fast-cooling phase. Since the coefficient of thermal expansion of silica is roughly six times smaller than  $\text{MoS}_2$  (refs 24,25), a fast-cooling process from the growth temperature ( $\sim 850^\circ\text{C}$ ) could create a significant contraction mismatch (Supplementary Discussion). As a result, the monolayer  $\text{MoS}_2$  triangles will be in tensile strain. Local strain variation regions extended from the edges vertically are towards the centre (Fig. 2d–f). In other words, after cooling, the CVD  $\text{MoS}_2$  monolayer triangles are under a tensile strain but contains localized regions where this strain has been partially released (less strained) possibly due to combined effects of geometry and inevitable variations in interactions with the substrate. To estimate this CVD growth-induced strain variations, density functional theory (DFT) calculations are performed and a relationship between the PL peak position shift and the strain variations in the sample is established (Fig. 2h). The corresponding difference in strain is estimated to be  $\sim 0.2\%$ . Although the DFT simulations do not account for the excitonic effects, the relative change of the calculated bandgap with respect to uniaxial strain ( $-44\text{ meV per } \%$  strain) matches quite well with previous experiments on the PL peak position shift with strain ( $-45\text{ meV per } \%$  strain<sup>26</sup> and  $-36\text{ meV per } \%$  strain<sup>27</sup>). Furthermore, as we mentioned, due to the fast cooling, a global tensile strain is found in  $\text{MoS}_2$ . To support our conjecture, we transfer  $\text{MoS}_2$  to a new  $\text{Si/SiO}_2$  substrate and compare the PL mapping. As expected, the tensile strain in the film as well as the local variations are released after the transfer process (Supplementary Figs 2 and 3). The global tensile strain is estimated to be  $\sim 1\%$ . This information provides insight into the role of thermal property mismatch between the substrate and  $\text{MoS}_2$  in the CVD process. Our observations suggest that PL studies can be effectively used as a strain-mapping tool and a tool to evaluate strain-induced bandgap engineering if an independent and robust link between the two parameters can be established. To further explore the role of substrate properties in  $\text{MoS}_2$  strain engineering, a well-controlled experiment is performed. This experiment will also correlate strain with optical and band structure properties of monolayer  $\text{MoS}_2$ .

## Bandgap engineering and effective strain transfer for $\text{MoS}_2$ .

Substrate-induced straining of 2D materials for band structure engineering has been effectively explored in previous studies<sup>26,28</sup>. However, these experiments have only been performed on exfoliated samples and a comprehensive study of the role of substrate and homogeneity on the transferred strain has not been explored. Most recently, the strain-induced bandgap changes in monolayer  $\text{MoS}_2$ , using polymer substrates, has been demonstrated<sup>26,28–30</sup>. However, because of the weak adhesion between  $\text{MoS}_2$  and substrates, strain cannot be completely transferred to  $\text{MoS}_2$  from the substrate, as exemplified in graphene strain-engineering studies<sup>31,32</sup>. Understanding how much strain is effectively transferred to the  $\text{MoS}_2$  samples becomes critical to bridge experimental data and theoretical calculations. In our work, monolayer  $\text{MoS}_2$  triangles have been transferred from  $\text{SiO}_2$  to PDMS ( $\sim 0.5\text{ mm}$  in thickness; Fig. 3a). As we discussed in Fig. 1 and Supplementary Fig. 2, through the transfer, the thermal mismatch induced tensile strain in  $\text{MoS}_2$  and related local strain variations are released. Uniaxial force is then applied to the sample in the direction indicated by the arrows in Fig. 3a,c and was directly observed since the  $\text{MoS}_2$  on PDMS is visible under optical microscopy (Fig. 3b). Deformation of  $\text{MoS}_2$  flakes is clearly seen after the application of force on the



**Figure 2 | Intrinsic tensile strain in single-crystal CVD MoS<sub>2</sub>.** (a–c) Raman and PL intensity mapping at the  $E_{2g}^1$ ,  $A_{1g}$  Raman vibrating modes and the strongest PL peak from the A exciton, respectively. Scalar bar, 3  $\mu\text{m}$ . (d–f) Raman and PL peak position mapping at the same vibrating modes. Scalar bar, 3  $\mu\text{m}$ . (g) PL spectra recorded from uniform strain (black) and strain-vibration locations (red). Inset shows a  $\sim 8$ -meV blue shift, corresponding to a reduced tensile strain (0.2% less) comparing with the location of uniform strain. (h) DFT calculations of bandgap shift of monolayer MoS<sub>2</sub> versus tensile strain. The dots represent energy shift under an increasing strain from DFT calculations and the trend is shown by the dash line.

PDMS (Fig. 3c, under 4.8% tensile strain). The PL intensity (Fig. 3d) and peak position (Fig. 3e) mapping were obtained for this sample under an increasing tensile strain from 0 to 4.8%. Individual PL spectra are shown in Fig. 3f. The corresponding energy shift and intensity versus tensile strain are plotted in Fig. 3g. It is worth noting that no hysteresis was observed for the loading and unloading processes, which exclude the possibility of sliding effect between MoS<sub>2</sub> and substrates (Supplementary Fig. 4).

It is apparent that not all of the applied strain to the PDMS substrate was transferred to MoS<sub>2</sub> crystals, if one were to compare the results from Figs 2g,h and 3f,g. The heterogeneity of PL at zero strain also suggests that the transfer process and PDMS surface properties result in a non-uniform contact between the substrate and material. To better explain the experimental results and estimate the strain transferred to MoS<sub>2</sub> layer under such tensile tests, a 3D FE model was developed, as schematically shown in Fig. 4. Due to the symmetry, one half of the triangular sample was used in the model, and the model consists of one monolayer MoS<sub>2</sub> with a thickness of 0.7 nm, placed on the surface of PDMS substrate with a thickness of 100  $\mu\text{m}$  (Fig. 4a–c).

Figure 4d–h shows the strain distribution in the triangular MoS<sub>2</sub> layer at different applied strains on PDMS. The tensile

strain is clearly transferred from the substrate to the MoS<sub>2</sub> layer. The strain transferred to MoS<sub>2</sub> layer initiates from the top of the triangle (point A in Fig. 4c) and then propagates down along the triangle and finally extends to the bottom. Interestingly, the predicted strain distribution across the MoS<sub>2</sub> is in good agreement with the PL peak position mapping shown in Fig. 3e, indicating that the PL peak position distribution is closely correlated to the local strain. The strains in MoS<sub>2</sub> layer as a function of the applied strain on PDMS are shown in Fig. 4i, where a linear relationship is predicted within the range of 5% at which the substrates have still not yielded under such applied strain levels. When the applied strain reaches 4.8%, as in the experiment, the strain in MoS<sub>2</sub> layer varies ranging from 0.50, 0.27 and 0.14% at points A, B and C (Fig. 4c), respectively. Thus, up to 10% of the applied strain has been effectively transferred to MoS<sub>2</sub> layer in the case of assuming perfect van der Waals bonding between the MoS<sub>2</sub> and the substrate. These results correlate well with the earlier PL peak position mapping of the CVD-grown MoS<sub>2</sub> crystal with strain variations and corresponding DFT calculations, confirming the validity of the proposed method for strain detection and bandgap engineering evaluation using the PL peak position mapping technique. They also demonstrate the role of substrate and crystal geometry.



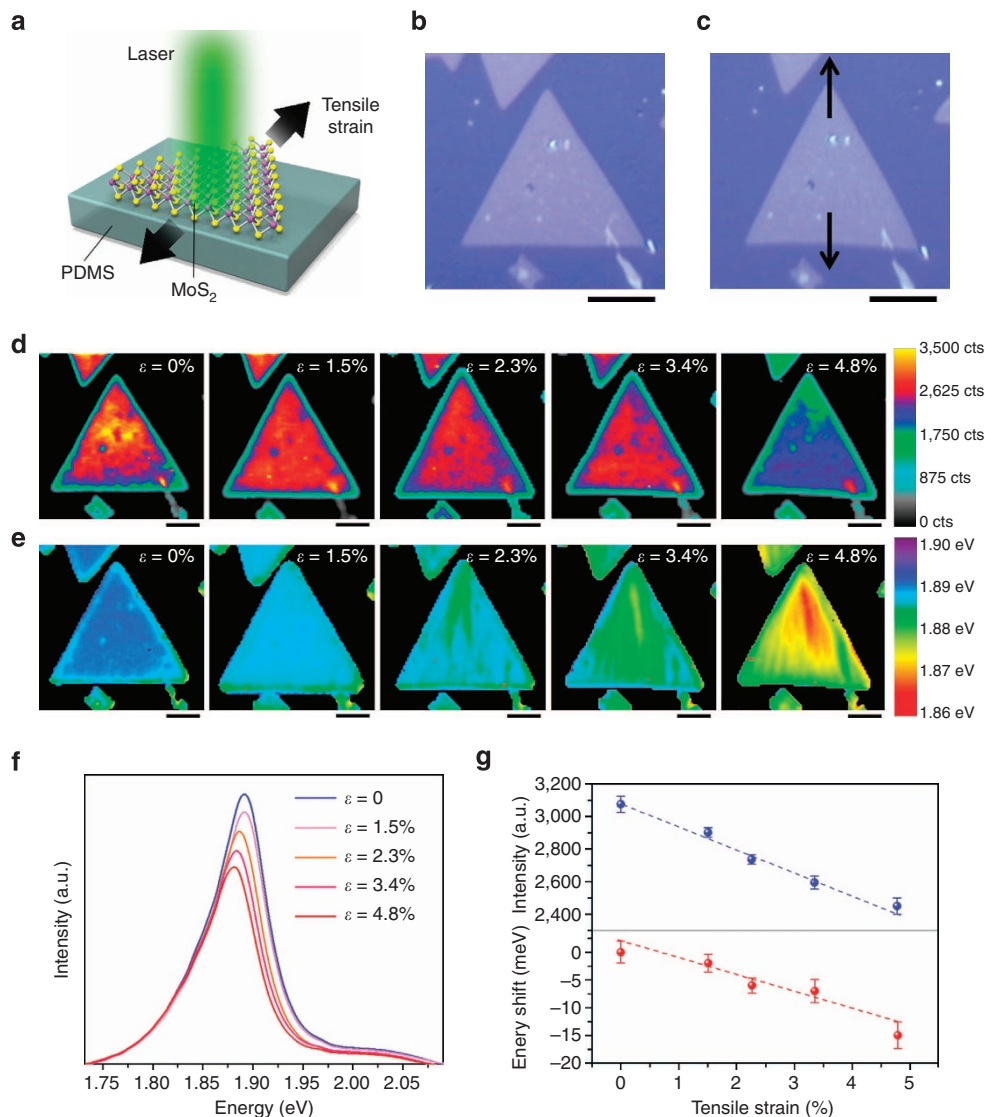


**Figure 3 | Controlled tensile strain in single-crystal CVD MoS<sub>2</sub>.** (a) Schematic of PDMS/MoS<sub>2</sub> stacks for tensile strain experiment. The uniaxial tensile force is applied along the direction of the black arrows, as indicated. (b,c) Optical images of MoS<sub>2</sub> without and under 4.8% strain, respectively. Black arrows show the direction of the applied force. Scalar bar, 6  $\mu$ m. (d,e) PL intensity and peak position mapping under an increasing tensile strain from 0 to 4.8%. Scalar bar, 4  $\mu$ m. (f) Representative PL spectra under each strain, collected from the centre of the triangle. (g) Energy shift (red) and intensity (blue) of the PL peak (strongest PL peak from the A exciton) versus the tensile strain of PDMS. Multiple spectra were recorded at each strain.

In addition, it is important to calculate the effective strain transfer from the polymer to MoS<sub>2</sub> and demonstrate how to promote the strain transfer for bandgap engineering. In our experiments, with 4.8% tensile strain applied to the PDMS substrate, only a 15-meV shift was observed in the PL spectra near the centre of the triangle, corresponding to  $\sim 0.5\%$  tensile strain according to DFT calculations. It should be noted here that DFT-LDA (local-density approximation) usually produces a relatively lower value than the true bandgap, yet the change in bandgap can be more accurately determined, although the absolute value is underestimated<sup>33</sup>. Our work suggests that only  $\sim 10\%$  of the applied strain is effectively transferred to MoS<sub>2</sub> when using PDMS as a substrate. Note that this strain transfer efficiency was also confirmed by the earlier FE simulation (Fig. 4). Therefore, it will be of practical importance to further investigate the strain loss mechanisms in such a system. We calculated the strain in the MoS<sub>2</sub> layer for various substrates with Young's modulus ranging from 0.35 KPa to 1 GPa. The maximum transfer strain versus Young's modulus is shown in Fig. 4j. If the Young's

modulus of a substrate is below 1 MPa, the transferred strain is about 0.5% for an applied strain of 5%. With the increasing substrate modulus, the transferred strain quickly increases to 4.7% for the same applied strain, indicating that almost 90% of the applied strain is transferred to the MoS<sub>2</sub> layer. As a controllable experiment, we transferred the MoS<sub>2</sub> to polyvinyl alcohol with Young's modulus around 650 MPa, around three orders of magnitude higher than PDMS ( $\sim 430$  KPa). It turns out  $\sim 60\%$  strain that has been effectively transferred to MoS<sub>2</sub> based on a linear extrapolation from Fig. 2h (Supplementary Fig. 5). This result supports our FE simulation predictions. Thus, increasing the substrate modulus could significantly increase the strain in MoS<sub>2</sub> layer if a high-quality interface is preserved. This result provides a very useful guideline for the fabrication of highly tunable MoS<sub>2</sub> electronic devices.

**Structural heterogeneity in CVD-grown MoS<sub>2</sub> monolayers.** In addition to strain heterogeneity, GBs are one of the most

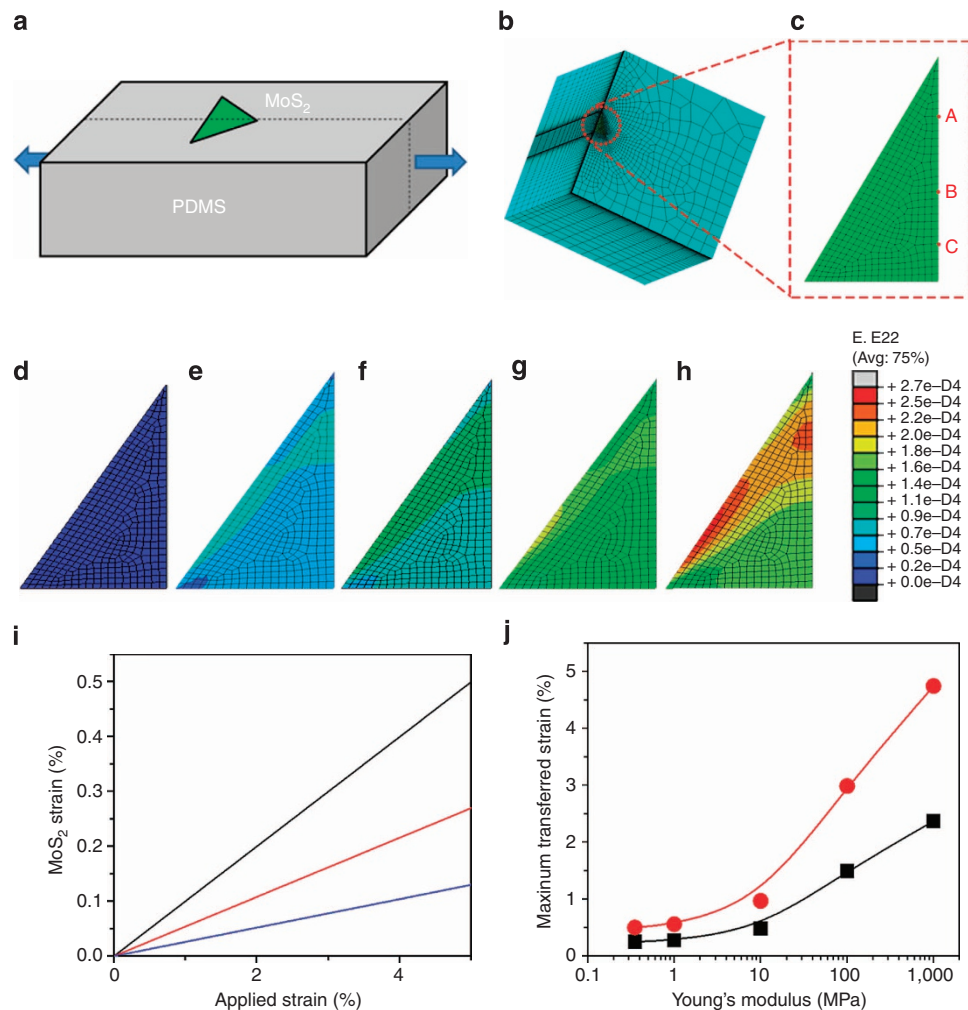


**Figure 4 | FE simulation of tensile-strained MoS<sub>2</sub>.** (a) Schematic of the tensile test sample, (b) FE model of the tensile test sample consisting of a 100- $\mu$ m-thick substrate (PDMS) and (c) a monolayer MoS<sub>2</sub> (0.7 nm) on the PDMS substrates. Half of the tensile test sample was modelled due to symmetry. (d–h) Snapshots of FEA simulation of MoS<sub>2</sub> tensile tests: applied strain (d) 0%, (e) 1.5%, (f) 2.2%, (g) 3.4% and (h) 4.8%. (i) Strain in MoS<sub>2</sub> layer as a function of the applied strain on the substrate at points A (black), B (red) and C (blue). (j) Maximum strain in MoS<sub>2</sub> layer as a function of substrate's Young's Modulus for 2.5% (black) and 5% (red) tensile strain.

significant structural features in CVD-grown polycrystalline MoS<sub>2</sub> samples as shown in Fig. 1b–d. Attempts to grow large-area crystals of MoS<sub>2</sub> has rendered an unavoidable polycrystallinity that calls for better and simpler identification method for detecting the GBs and understanding their role in the electronic and optical properties of the material. The experimental and theoretical work on the GBs of MoS<sub>2</sub> has revealed a rich diversity in their structure<sup>19,21</sup>. It is known that monolayer MoS<sub>2</sub> has a hexagonal lattice structure similar to graphene and h-BN. However, in contrast to single-atom-thick graphene, MoS<sub>2</sub> monolayers consist of two layers of sulfur atoms sandwiching a layer of molybdenum atoms. This results in a variety of dislocation cores, constituting the grain boundary configurations in MoS<sub>2</sub>, as opposed to the most common 5–7 ring configuration in graphene<sup>34</sup>. In addition, variations in the lattice orientation mismatch at the boundaries and non-bonding second-layer growth are common features observed in CVD-grown large-area MoS<sub>2</sub> films<sup>4</sup>. It was also found that the twin GB in MoS<sub>2</sub> may exhibit metallic behaviour<sup>21</sup>. The most reliable method for identification of GBs has traditionally been the high-resolution TEM techniques, which can directly inspect its detailed atomic structural characteristics. This approach provides a unique atomic-level perspective of the MoS<sub>2</sub> boundaries, but is

not suitable for direct examination of large-area samples/devices that are ready for subsequent optical and electrical measurements. Consequently, optical-based microscopy techniques for identification and characterization of GBs have been explored using high-resolution PL mapping.

Non-contact optical techniques such as Raman spectroscopy can be employed to map the GBs of graphene. Since the Raman spectra for MoS<sub>2</sub> is very sensitive to the number of layers, it has been proposed as a suitable approach for detection of over-layered MoS<sub>2</sub> GBs (Supplementary Fig. 6). Nevertheless, for monolayer MoS<sub>2</sub>, this technique is not efficient in detecting GBs because the Raman signal is very weak and strongly dependent on the laser power for monolayer MoS<sub>2</sub>. PL variations at the GB have also been explored; however, little is known about the fundamental reasons for the observed changes. As discussed earlier, the PL peak position mapping is proven to be an effective method to detect intrinsic strains in monolayer MoS<sub>2</sub> (ref. 21). It is well known that the grain boundary in 2D material consists of lined-up dislocations, which naturally may introduce localized strain in their vicinity. In addition, the variety in CVD-grown crystal geometries and grain boundary types can be utilized to further gather insight into their role in MoS<sub>2</sub> PL characteristics.

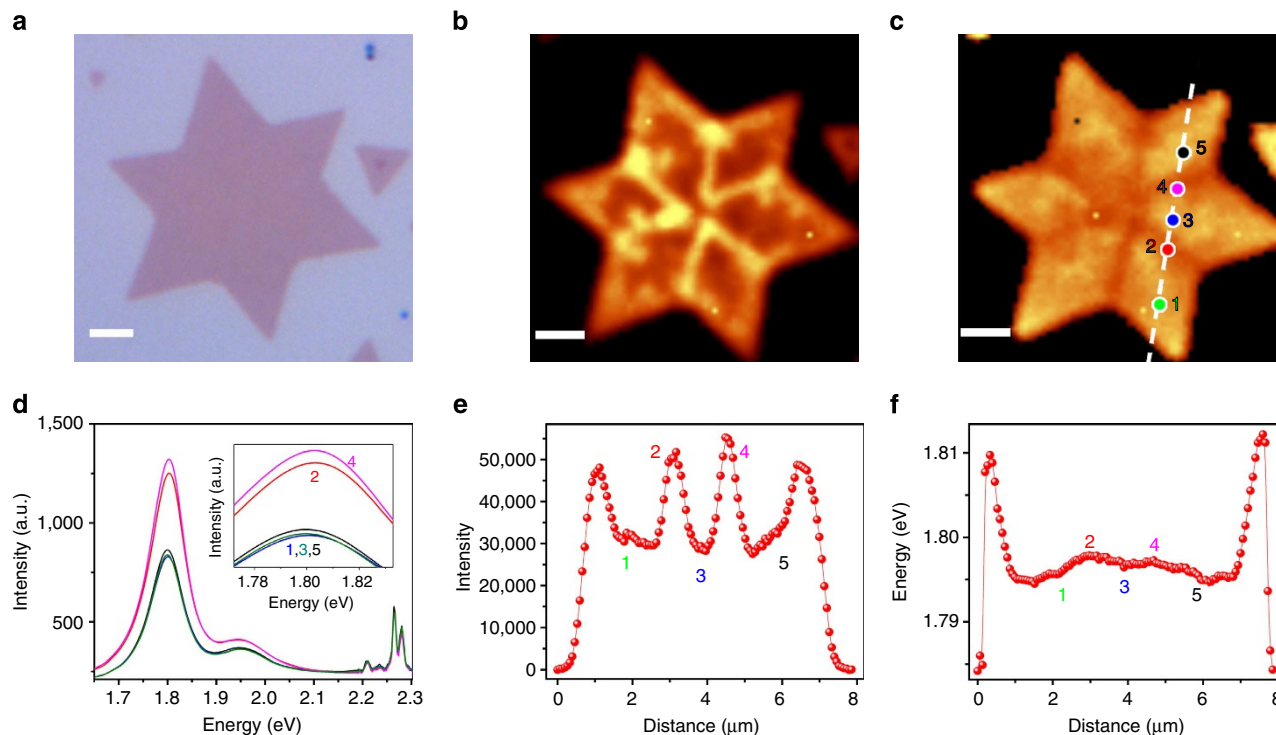


**Figure 5 | PL characterization of polycrystalline MoS<sub>2</sub> star with twin GBs.** (a) Optical image of a MoS<sub>2</sub> star sitting on SiO<sub>2</sub>. (b) PL intensity mapping. The edges and twin GBs have a higher intensity (light yellow), while rest are depicted in orange. (c) PL peak position mapping. PL spectra are collected at the location marked five dots with different colours. (d) PL spectra collected from points indicated in c. Each spectrum corresponds to the location in c with the same color. (e,f) PL intensity and peak position line profiles as indicated by the white dash lines crossing two GBs and two edges.

To analyse the PL response of GBs in polycrystalline MoS<sub>2</sub>, we examine a representative six-pointed MoS<sub>2</sub> star with six twin GBs (Fig. 5a). The PL intensity mapping (Fig. 5b) reveals the enhanced intensity characteristics of six mirror-twin GBs. Such twin structures have also been confirmed by the PL peak position mapping (Fig. 5c). The same structure has been observed under dark-field TEM<sup>3</sup>. It was found that the outer edges are oriented along the Mo-z-z (molybdenum zigzag) direction, while GBs occur along the S-z-z (sulfur zigzag) direction (Supplementary Fig. 7)<sup>3</sup>. Nevertheless, these GBs represent unique defect characteristics. PL line profiles and five individual PL spectrums along the lines indicated in their respective scans are recorded (Fig. 5d–f). Their locations are labelled in Fig. 5c. Three of the points are located at the pristine MoS<sub>2</sub> and two of them at the GBs. An enhancement in the PL up to 250% is observed at the GBs (Fig. 5d,e). The highest PL intensity is found at the GBs and edges, which is opposite to the report from Van der Zande *et al.*<sup>3</sup> who observed a lower PL intensity along the GBs in monolayer MoS<sub>2</sub>. The physical scenario of PL along the GBs is very complicated. According to previous studies, defects at the edges and the GBs may contribute the enhancement of PL intensity. New sub-bandgap emission peak as well as increase in overall PL intensity were found as a result of the vacancy generation<sup>35</sup> via a defect-assisted process<sup>36</sup>. Here, our results also imply that a local interaction also plays an important role in the PL variations. We propose that the non-uniform strain due to the thermal mismatch of the substrate, randomness of interface properties and strain transfer and tensile straining native to GBs combined make the most significant contribution to the optical bandgap shifts. We find that, in Fig. 5, the PL peak shift is ~5 meV at the GBs and ~15 meV at the edges in monolayer MoS<sub>2</sub>. This small blue shift indicates that no matter what type of defects exist at the GBs, their behaviour tends to be very similar. This further supports our

hypothesis that strain at the GBs is possibly the main reason for the observation of changes in the PL characteristics of MoS<sub>2</sub>. To confirm the strain in GBs, we collected low-temperature PL spectra at non-GB and GB locations. The shifts have been found for both locations and the difference in peak location increases, demonstrating that the PL spectra at the GBs are more sensitive to the change of strain (Supplementary Fig. 8). We have examined the temperature dependency of the bandgap and PL positions of MoS<sub>2</sub> atomic layers using a modified Varshni model (Supplementary Fig. 8)<sup>37</sup>. These results show a good fit for the measurement of the optical gap in the crystalline region and the grain boundary regions of MoS<sub>2</sub>, implying that the changes seen in the PL characteristics are not results of disorder and localizations in the excitonic transitions. Also, not only for the symmetric MoS<sub>2</sub> stars, similar results have been seen from the asymmetric polycrystalline MoS<sub>2</sub> flakes with GBs (Supplementary Fig. 9). In addition, we have also noticed that, in some MoS<sub>2</sub> polycrystalline flakes, the GBs were broken induced by tensile strain. It further confirms the vulnerability of GBs in MoS<sub>2</sub> (Supplementary Fig. 10) and the impact of strain.

## Discussion

In this work, we have used PL mapping to study strain and structural heterogeneity in PL characteristics of CVD-grown MoS<sub>2</sub> monolayers. We observe and quantify the native non-uniform strain in such samples and propose that the difference in thermal expansion coefficient of MoS<sub>2</sub> and the supporting SiO<sub>2</sub> substrate leads to an intrinsic tensile strain in MoS<sub>2</sub> during the fast-cooling process at the final stage of the growth. A relationship between the PL peak position shifts and strain is established and can be used for strain detection and bandgap engineering evaluation. Further examination of substrate-mediated straining



process provides important insight into the role of substrate in effective strain transfer. Through FE simulation and controlled tensile experiments, we find that for PDMS substrates only  $\sim 10\%$  of the applied strain can be effectively transferred to MoS<sub>2</sub>. Moreover, we demonstrate how strain concentration propagates in a triangular MoS<sub>2</sub> monolayer crystal and propose substrates' Young's modulus as dominating mechanisms of strain loss. A substrate with a modulus  $> 1$  GPa may effectively transfer almost 90% of the applied strain to monolayer MoS<sub>2</sub> when perfect interfacial contact conditions are provided. In addition, we examine the discrepancies in the literature about the role of GBs in PL characteristics of MoS<sub>2</sub>. Our results suggest that thermally induced non-uniform tensile strain plays a significant role in grain boundary optical properties. Our results also provide a promising way for fabrication and study of highly tunable MoS<sub>2</sub> electronic devices and mechanisms of strain transfer in 2D atomic layers.

## Methods

**CVD of monolayer MoS<sub>2</sub>.** To synthesize MoS<sub>2</sub>, the precursors, MoO<sub>3</sub> films, were prepared through the filtration of their highly crystalline nanoribbons. These ribbons were produced hydrothermally through a process widely used for synthesis of this type of single-crystalline material. Sodium molybdate (Na<sub>2</sub>MoO<sub>4</sub>) or hexaammonium heptamolybdate tetrahydrate (NH<sub>4</sub>)<sub>6</sub>Mo<sub>7</sub>O<sub>24</sub> · 4H<sub>2</sub>O was used as precursors for the preparation of MoO<sub>3</sub> nanoribbons. We dissolve 1.2 g of these precursors in nitric acid and transfer to a Teflon container and heat it at 170 °C for 1–2 h. These MoO<sub>3</sub> nanoribbons have a high aspect ratio, roughly 20 μm in length, 1–2 μm in width and thickness in the range of 10–40 nm. After the preparation of these MoO<sub>3</sub> precursors, the ribbons were filtered, and large-area films were formed, cut into pieces and dispersed on silicon substrates. Several bare and clean substrates, designate for the growth of MoS<sub>2</sub>, and the MoO<sub>3</sub> film were placed close to each other at the centre of the furnace vented with nitrogen at 200 sccm. A container was filled with 0.8–1.2 g of sublimated sulfur and placed at the opening of the furnace at a location that reaches an approximately maximum temperature of 600 °C. The heating procedure corresponding to the temperature at the centre of the furnace starts with a gradual heating from room temperature to 550 °C in 30 min at a rate of  $\sim 20^\circ\text{C min}^{-1}$ . Then, at a slower pace,  $\sim 5^\circ\text{C min}^{-1}$ , the chamber is heated to 850 °C. After 10–15 min at this temperature, the furnace is cooled naturally back to room temperature. At temperatures close to 550 °C at the centre, sulfur will slowly start to evaporate and the central interaction between this element and MoO<sub>3</sub> follows.

Both Raman and PL data were collected using a 532-nm laser excitation focused through a  $\times 100$  objective lens. This resulted in a spot size of  $\sim 342$  nm where scanning was performed using 200 nm steps on a piezoelectric stage to obtain high-resolution images. All Raman and PL spectra presented in this manuscript for MoS<sub>2</sub> on SiO<sub>2</sub>/Si were taken at an incident laser power of 12.5 μW, which was sufficiently low to avoid any shifting of the Raman modes during scanning. Mapping on the PDMS substrate was performed at an incident laser power of 50 μW to improve the signal to noise ratio. The PL peak position was found to be much less sensitive to the laser power density. Specifically, the laser power dependence on Raman peak position and intensity is shown in Supplementary Figs 11 and 12 and shows that the layer number can easily be incorrectly determined when scanning at high power densities.

**DFT calculations.** DFT calculations within the LDA were performed using the projector-augmented wave (PAW) method<sup>38,39</sup>, as implemented in Vienna Ab-initio Simulation Package<sup>40,41</sup>. Twelve electrons were included for Mo pseudopotential. A vacuum layer  $> 12$  Å was introduced to make the spurious interactions negligible. A  $11 \times 11 \times 1$  Monkhorst-Pack  $k$ -point mesh centred at the  $\Gamma$ -point was adopted for the Brillouin zone integration. With an energy cutoff of 280 eV, a plane-wave-based total energy minimization scheme<sup>42</sup> was employed until the force on each atom was  $< 0.01$  eV Å<sup>-1</sup>. The uniaxial strain was applied either in the armchair (AC) or zigzag (ZZ) direction.

**3D FEA.** The discretized FE models contain about 53,254 nodes and 49,584 elements with very fine meshes in the contact region. The final mesh density was determined through a series of convergence studies. Appropriate boundary conditions were used along two edges of the specimen to simulate the loading strain during testing. The interface between MoS<sub>2</sub> and PDMS were modelled using perfect bonding. The calculations were performed using the commercial FE package ABAQUS (version 6.10). Young's modulus and Poisson's ratio for PDMS are 350 KPa and 0.5, and 300 GPa and 0.3, respectively, were used in the simulation.

## References

- Zhan, Y., Liu, Z., Najmaei, S., Ajayan, P. M. & Lou, J. Large-area vapor-phase growth and characterization of MoS<sub>2</sub> atomic layers on a SiO<sub>2</sub> substrate. *Small* **8**, 966–971 (2012).
- Yu, Y. *et al.* Controlled scalable synthesis of uniform, high-quality monolayer and few-layer MoS<sub>2</sub> films. *Sci. Rep.* **3**, 1866 (2013).
- van der Zande, A. M. *et al.* Grains and grain boundaries in highly crystalline monolayer molybdenum disulfide. *Nat. Mater.* **12**, 554–561 (2013).
- Najmaei, S. *et al.* Vapour phase growth and grain boundary structure of molybdenum disulfide atomic layers. *Nat. Mater.* **12**, 754–759 (2013).
- Lee, Y.-H. *et al.* Synthesis and transfer of single-layer transition metal disulfides on diverse surfaces. *Nano Lett.* **13**, 1852–1857 (2013).
- Wang, X., Feng, H., Wu, Y. & Jiao, L. Controlled synthesis of highly crystalline MoS<sub>2</sub> flakes by chemical vapor deposition. *J. Am. Chem. Soc.* **135**, 5304–5307 (2013).
- Jariwala, D., Sangwan, V. K., Lauhon, L. J., Marks, T. J. & Hersam, M. C. Emerging device applications for semiconducting two-dimensional transition metal dichalcogenides. *ACS Nano* **8**, 1102–1120 (2014).
- Huang, X., Zeng, Z. & Zhang, H. Metal dichalcogenide nanosheets: preparation, properties and applications. *Chem. Soc. Rev.* **42**, 1934–1946 (2013).
- Chhowalla, M. *et al.* The chemistry of two-dimensional layered transition metal dichalcogenide nanosheets. *Nat. Chem.* **5**, 263–275 (2013).
- Li, Y. *et al.* MoS<sub>2</sub> nanoparticles grown on graphene: an advanced catalyst for the hydrogen evolution reaction. *J. Am. Chem. Soc.* **133**, 7296–7299 (2011).
- Cao, L. *et al.* Direct laser-patterned micro-supercapacitors from paintable MoS<sub>2</sub> films. *Small* **9**, 2905–2910 (2013).
- Radisavljevic, B., Radenovic, A., Brivio, J., Giacometti, V. & Kis, A. Single-layer MoS<sub>2</sub> transistors. *Nat. Nanotechnol.* **6**, 147–150 (2011).
- Yin, Z. *et al.* Single-layer MoS<sub>2</sub> phototransistors. *ACS Nano* **6**, 74–80 (2011).
- Zeng, H., Dai, J., Yao, W., Xiao, D. & Cui, X. Valley polarization in MoS<sub>2</sub> monolayers by optical pumping. *Nat. Nanotechnol.* **7**, 490–493 (2012).
- Kumar, N. *et al.* Second harmonic microscopy of monolayer MoS<sub>2</sub>. *Phys. Rev. B* **87**, 161403 (2013).
- Zhu, C. *et al.* Single-layer MoS<sub>2</sub>-based nanopores for homogeneous detection of biomolecules. *J. Am. Chem. Soc.* **135**, 5998–6001 (2013).
- Lee, Y.-H. *et al.* Synthesis of large-area MoS<sub>2</sub> atomic layers with chemical vapor deposition. *Adv. Mater.* **24**, 2320–2325 (2012).
- Lin, J. *et al.* 3-Dimensional graphene carbon nanotube carpet-based microsupercapacitors with high electrochemical performance. *Nano Lett.* **13**, 72–78 (2012).
- Zou, X., Liu, Y. & Jakobson, B. I. Predicting dislocations and grain boundaries in two-dimensional metal-disulfides from the first principles. *Nano Lett.* **13**, 253–258 (2012).
- Yu, Y. *et al.* Controlled scalable synthesis of uniform, high-quality monolayer and few-layer MoS<sub>2</sub> films. *Sci. Rep.* **3**, 1866 (2013).
- Zhou, W. *et al.* Intrinsic structural defects in monolayer molybdenum disulfide. *Nano Lett.* **13**, 2615–2622 (2013).
- Splendiani, A. *et al.* Emerging photoluminescence in monolayer MoS<sub>2</sub>. *Nano Lett.* **10**, 1271–1275 (2010).
- Eda, G. *et al.* Photoluminescence from chemically exfoliated MoS<sub>2</sub>. *Nano Lett.* **11**, 5111–5116 (2011).
- El-Kareh, B. in *Fundamentals of Semiconductor Processing Technology* (Springer, 1995).
- El-Mahalawy, S. H. & Evans, B. L. The thermal expansion of 2H-MoS<sub>2</sub>, 2H-MoSe<sub>2</sub> and 2H-WSe<sub>2</sub> between 20 and 800 degrees C. *J. Appl. Crystallogr.* **9**, 403–406 (1976).
- Conley, H. J. *et al.* Bandgap engineering of strained monolayer and bilayer MoS<sub>2</sub>. *Nano Lett.* **13**, 3626–3630 (2013).
- Castellanos-Gomez, A. *et al.* Local strain engineering in atomically thin MoS<sub>2</sub>. *Nano Lett.* **13**, 5361–5366 (2013).
- Hui, Y. Y. *et al.* Exceptional tunability of band energy in a compressively strained trilayer MoS<sub>2</sub> sheet. *ACS Nano* **7**, 7126–7131 (2013).
- He, K., Poole, C., Mak, K. F. & Shan, J. Experimental demonstration of continuous electronic structure tuning via strain in atomically thin MoS<sub>2</sub>. *Nano Lett.* **13**, 2931–2936 (2013).
- Wang, Y., Cong, C., Qiu, C. & Yu, T. Raman spectroscopy study of lattice vibration and crystallographic orientation of monolayer MoS<sub>2</sub> under uniaxial strain. *Small* **9**, 2857–2861 (2013).
- Jiang, T., Huang, R. & Zhu, Y. Interfacial sliding and buckling of monolayer graphene on a stretchable substrate. *Adv. Funct. Mater.* **24**, 396–402 (2013).
- Ni, Z. H. *et al.* Uniaxial strain on graphene: Raman spectroscopy study and band-gap opening. *ACS Nano* **2**, 2301–2305 (2008).
- Shi, H., Pan, H., Zhang, Y.-W. & Jakobson, B. I. Quasiparticle band structures and optical properties of strained monolayer MoS<sub>2</sub> and WS<sub>2</sub>. *Phys. Rev. B* **87**, 155304 (2013).
- Huang, P. Y. *et al.* Grains and grain boundaries in single-layer graphene atomic patchwork quilts. *Nature* **469**, 389–392 (2011).



35. Tongay, S. *et al.* Defects activated photoluminescence in two-dimensional semiconductors: interplay between bound, charged, and free excitons. *Sci. Rep.* **3**, 2657 (2013).
36. Korn, T., Heydrich, S., Hirmer, M., Schmutzler, J. & Schuller, C. Low-temperature photocarrier dynamics in monolayer MoS<sub>2</sub>. *Appl. Phys. Lett.* **99**, 102103–102109 (2011).
37. O'Donnell, K. P. & Chen, X. Temperature dependence of semiconductor band gaps. *Appl. Phys. Lett.* **58**, 2924–2926 (1991).
38. Blöchl, P. E. Projector augmented-wave method. *Phys. Rev. B* **50**, 17953–17979 (1994).
39. Kresse, G. & Joubert, D. From ultrasoft pseudopotentials to the projector augmented-wave method. *Phys. Rev. B* **59**, 1758–1775 (1999).
40. Kresse, G. & Furthmüller, J. Efficient iterative schemes for ab initio total-energy calculations using a plane-wave basis set. *Phys. Rev. B* **54**, 11169–11186 (1996).
41. Kresse, G. & Furthmüller, J. Efficiency of ab-initio total energy calculations for metals and semiconductors using a plane-wave basis set. *Comput. Mater. Sci.* **6**, 15–50 (1996).
42. Ihm, J., Zunger, A. & Cohen, M. L. Momentum-space formalism for the total energy of solids. *J. Phys. C* **12**, 4409–4422 (1979).

## Acknowledgements

This work was supported by the Welch Foundation grant C-1716, the NSF grant ECCS-1327093, the U.S. Army Research Office MURI grant W911NF-11-1-0362, the U.S. Army Research Lab (ARL) Director's Strategic Initiative (DSI) program on interfaces in stacked 2D atomic layered materials, the U.S. Office of Naval Research MURI grant N000014-09-1-1066, the Nanoelectronics Research Corporation contract S201006, a Wigner Fellowship through the Laboratory Directed Research and Development Program of Oak Ridge National Laboratory, managed by UT-Battelle, LLC, for the U.S. DOE (W.Z.), and through a user project supported by ORNL's Center for Nanophase Materials Sciences (CNMS), which is sponsored by the Scientific User Facilities Division,

Office of Basic Energy Sciences, U.S. DOE. This work was also supported in part by the FAME Center, one of six centres of STARnet, a Semiconductor Research Corporation program sponsored by MARCO and DARPA. This work was also supported by the Singapore National Research Foundation under NRF RF Award No. NRF-RF2013-08, the start-up funding from Nanyang Technological University (M4081137.070). The computations were performed at the Cyberinfrastructure for Computational Research funded by NSF under Grant CNS-0821727 and the Data Analysis and Visualization Cyberinfrastructure funded by NSF under Grant OCI-0959097.

## Author contributions

Z.L., M.A. and S.N. contributed equally to this work. Z.L., M.A., A.G.B. and J.L. designed the experiments. Z.L., M.A. and A.G.B. carried out most of the PL and Raman characterizations and analysed the data. S.N. worked on the CVD growth of MoS<sub>2</sub> and PL strain experiments. Q.X. and Z.X. performed the FEA simulation. X.Z. and B.I.Y. worked on the DFT calculation. W.Z. carried out STEM experiments. T.Y. and C.Q. conducted the PL characterizations for part of the samples and data analysis. Z.L., M.A., S.N., Q.X., Z.X., W.Z. and J.L. co-wrote the paper. All the authors discussed the results.

## Additional information

**Supplementary Information** accompanies this paper at <http://www.nature.com/naturecommunications>

**Competing financial interests:** The authors declare no competing financial interests.

**Reprints and permission** information is available online at <http://npg.nature.com/reprintsandpermissions/>

**How to cite this article:** Liu, Z. *et al.* Strain and structure heterogeneity in MoS<sub>2</sub> atomic layers grown by chemical vapour deposition. *Nat. Commun.* **5**:5246 doi: 10.1038/ncomms6246 (2014).